Available online at www.sciencedirect.com
ScienceDirect
Journal of Sound and Vibration 323 (2009) 1045–1060
JOURNAL OF SOUND AND VIBRATION
www.elsevier.com/locate/jsvi

Dynamic response of a rotating multi-span shaft with general boundary conditions subjected to a moving load

T.N. Shiau[a,*], K.H. Huang[a], F.C. Wang[a], W.C. Hsu[b]

[a]*Department of Mechanical Engineering, National Chung Cheng University, 621 Chia-Yi, Taiwan, ROC*
[b]*Department of Mechanical Engineering, Wu Feng Institute of Technology, 621 Chia-Yi, Taiwan, ROC*

Received 13 July 2008; received in revised form 8 January 2009; accepted 18 January 2009
Handling Editor: L.G. Tham
Available online 6 March 2009

Abstract

This paper investigates the dynamic response of a rotating multi-span shaft with general boundary conditions subjected to an axially moving load. The system equations of motion are derived based on the global assumed mode method and a modified transformation matrix is proposed to deal with the multi-span geometric constraints. The numerical results are solved by the Runge–Kutta method. To ensure the validity of the method, the convergence test for dynamic response and the comparison of natural frequencies obtained by both the present method and finite element method are demonstrated. Numerical simulations are performed to study the effects of the moving speed of the load, the number of spans, and the rotational speed of the shaft on the deflections under the moving load. In addition, the effects on the occurring position of maximum deflection are presented. The numerical results show that the maximum deflection in the direction of the load may occur at any span and near the midpoint of one span. However, the maximum deflection induced by the gyroscopic effect in the direction perpendicular to the load always occurs at the first span. Moreover, the occurring position of maximum deflection is independent of the rotational speed.

1. Introduction

The dynamic behavior of a beam subjected to moving loads has been extensively studied. Based on the proposed system models, the configurations can be categorized as non-rotating beam or rotating beam, uniform beam or non-uniform beam, single-span or multi-span. And the types of loads acting on the beam include constant force, harmonic force, deflection dependent force, random force, and so on. However, there are only a few studies on the rotating beam model. Moreover, those studies only considered a single-span and focused on the effects of various boundary conditions and types of applied force on the dynamic response.

Katz et al. [1] analyzed the dynamic response of a simply supported shaft subjected to a lateral force with constant velocity and magnitude moving axially along the shaft. The effects of the rotational speed, moving speed and shaft geometry were studied and the numerical results were presented based on Euler–Bernoulli,

*Corresponding author. Tel.: +886 5 2720411x33317; fax: +886 5 2724004.
E-mail address: imetls@ccu.edu.tw (T.N. Shiau).

0022-460X/$ - see front matter © 2009 Elsevier Ltd. All rights reserved.
doi:10.1016/j.jsv.2009.01.034

Rayleigh, and Timoshenko beam models. Zu and Han [2] developed a modal analysis approach with adjoint differential matrix operator for solving the problem of Ref. [1] and studied the dynamic responses with general boundary conditions. In addition to a lateral moving force, Lee [3] considered the axial nonmoving compressive forces acting on the ends of the shaft and indicated that the effect caused the deflection of the shaft to increase and fluctuate significantly. Shiau et al. [4] further investigated the effect of an axial moving compressive force on the dynamic response of a shaft. Zibdeh and Juma [5] treated the moving load as a random force and compared the dynamic responses with various beam theories and slenderness ratios. Argento and Scott [6] considered an accelerating distributed surface force and gave a comparison of dynamic responses obtained with constant velocity and acceleration. El-Saeidy [7] considered nonlinear end conditions arisen from nonlinear rolling bearings supporting a rotating shaft due to both the nonlinear stiffness and clearance. He applied the finite element method (FEM)to study the dynamic response of a rotating or non-rotating beam with or without nonlinear boundary conditions and subjected to a moving constant load. Ouyang and Wang [8] presented a dynamic model for the dynamic response of a shaft subjected to a three-direction moving load consisting of a lateral force, an axial force and a bending moment. The numerical results showed that the moving bending moment still affected the dynamic response significantly, although the moving speed and axial force were smaller. Argento and Morano [9,10] as well as Huang and Chang [11] studied the dynamic behavior of a shaft subjected to a moving deflection dependent load. The load represents the cutting force varying in the turning process since the workpiece vibration in the direction of the tool affects the actual depth of cut. They investigated the effects of cutting parameters and moving speed of the load on dynamic response and stability. Also, Guo and Han [12] employed the same approach of Ref. [1] to analyze the deflection of a shaft induced by the moving deflection dependent loads consisting of the radial and tangential components of a cutting force. They further predicted the diametral errors of the shaft from the geometric analysis of deflection of the shaft in both the radial and tangential directions. Yuan et al. [13] proposed a system model, which included the grinding wheel, the drive motor, and the roll modeled as an Euler–Bernoulli beam with simply supports, to simulate the paper machine roll grinding process. They introduced the regenerative effect, i.e. the time-delay effect arisen from the wavelike profile on the grinding wheel surface, into the system equations of motion and analyzed the dynamic response of a shaft in grinding.

All the aforementioned researches focused on the system model which described a rotating single-span shaft with general boundary conditions and investigated the effects of the various applied force types on dynamic response. However, in regard to the slender shaft, the steady rests is necessarily used to support the shaft for raising the system stiffness. In order to simplify the configuration of system, the steady rests can be modeled as the hinged supports and are placed between the two ends of the shaft. Thus the system model with a multi-span shaft has to be considered. Generally, the FEM [7], Galerkin's method (GM) [9–11], and mode superposition method (MSM) [1–6,8,12,13] were employed to analyze the dynamic response of a single-span shaft. However, in terms of a multi-span shaft, the mode shape functions satisfying the geometric constraints are difficult to obtain for the GM or MSM. Although the FEM can be easily applied for the model of a multi-span shaft, it requires the extensive computational time and computer memory due to its large dimension of system matrices. To solve those problems, the global assumed mode method (GAMM) proposed by Shiau and Hwang [14] is employed in this study. The mode shape functions used by GAMM are chosen as a series of polynomial functions, which are a set of arbitrary functions rather than admissible functions, comparison functions or eigenfunctions. Shiau et al. [15] introduced the transformation matrix constraining the boundaries of a single-span shaft to force the equations of motion to satisfy the geometric requirements. They successfully applied it to analyze the dynamic response of a single-span shaft with general boundary conditions.

In this study, a modified transformation matrix is proposed to deal with the multi-span geometric constraints including boundary conditions and intermediate supports. Then the GAMM together with the modified transformation matrix is employed to analyze the dynamic response of a multi-span shaft with general boundary conditions and subjected to a moving load. To ensure the validity of the method, a comparison of natural frequencies obtained by both the present method and FEM is given and the convergence test for dynamic response is performed. Furthermore, the effects of moving speed, rotational speed and number of spans on the deflection under the moving load and on the occurring position of maximum deflection are studied.

2. System equations of motion

Fig. 1 shows the configuration of a rotating simply supported shaft. A fixed reference frame X–Y–Z and a rotating reference frame x–y–z are utilized to describe the system motion. The X and x axes are collinear. The two reference frames have a single rotation ωt difference about X axis, where ω denotes a whirl speed. It is assumed that all the deflections and forces are parallel to the Y–Z plane. P_v and P_w represent the two components of the moving load acting on the shaft in Y and Z directions, respectively, and move from the right end of the shaft. This study considers a uniform shaft with small slenderness ratio and neglects the shear deflection. As indicated by Cheng and Lin [17], when the slenderness ratio, i.e. the Rayleigh beam coefficient, does not exceed 0.1, the Rayleigh beam model can be acceptable. Thus the flexible shaft is approximated by the Rayleigh beam model in this study. The deflection of a cross-section of flexible shaft consists of two translations V, W and two rotations B, Γ, which can be expressed as functions of position along the rotating axis x and time t:

$$V = V(x,t), \quad W = W(x,t),$$

$$B = B(x,t), \quad \Gamma = \Gamma(x,t). \tag{1}$$

The rotations B, Γ are related to the translations V, W by the equations,

$$B(x,t) = -\frac{\partial W(x,t)}{\partial x}, \quad \Gamma(x,t) = \frac{\partial V(x,t)}{\partial x}. \tag{2}$$

Using the GAMM, the associated deflections can be represented as

$$V(x,t) = \sum_{m=1}^{N_p} \phi_m(x) a_m(t), \quad W(x,t) = \sum_{n=1}^{N_p} \phi_n(x) b_n(t),$$

$$B(x,t) = -\sum_{n=1}^{N_p} \phi_n'(x) b_n(t), \quad \Gamma(x,t) = \sum_{m=1}^{N_p} \phi_m'(x) a_m(t), \tag{3}$$

where N_p is the number of mode shape functions. The time dependent coefficients a_m and b_n are generalized coordinates with respect to displacements V, Γ and W, B, respectively. The corresponding mode shape functions ϕ_m and ϕ_n are chosen as a series of polynomial functions:

$$\phi_m(x) = x^{m-1}, \quad m = 1,2,\ldots,N_p,$$

$$\phi_n(x) = x^{n-1}, \quad n = 1,2,\ldots,N_p. \tag{4}$$

The derivation of equations of motion requires the establishment of the equations which express the kinetic and potential energy of the system in terms of the displacements and their derivatives. Thus, the kinetic energy T_e [16], which includes the translational and rotational motions as well as the gyroscopic effect, is given by

$$T_e = \frac{1}{2}\int_0^l \rho A(\dot{V}^2 + \dot{W}^2)\,\mathrm{d}x + \frac{1}{2}\int_0^l \rho I(\dot{B}^2 + \dot{\Gamma}^2)\,\mathrm{d}x + \rho I l \Omega^2 + 2\Omega \int_0^l \rho I(\dot{B}\Gamma)\,\mathrm{d}x. \tag{5}$$

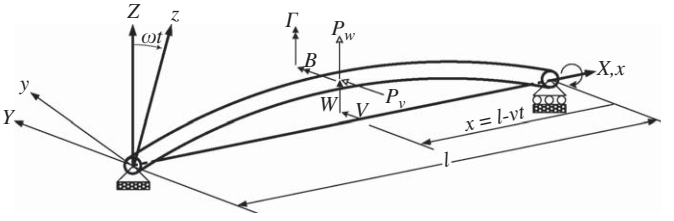

Fig. 1. The configuration and coordinates of a rotating simply supported shaft.

The potential energy U_e due to the pure bending is represented as

$$U_e = \frac{1}{2}\int_0^l EI[(V'')^2 + (W'')^2]\,\mathrm{d}x, \tag{6}$$

where the flexible shaft is of total length l with the distributed parameters of bending stiffness EI and mass per unit length ρA. Then the virtual work done by the moving loads for the system can be expressed as

$$\delta W_{ork} = P_v \sum_{m=1}^{N_p} \phi_m(x)\delta a_m + P_w \sum_{n=1}^{N_p} \phi_n(x)\delta b_n. \tag{7}$$

The Lagrangian approach is applied to obtain the governing equations of motion of the system as follows:

$$\sum_{m=1}^{N_p}\left\{\int_0^l \rho A\phi_m\phi_n\,\mathrm{d}x\ddot{a}_m + \int_0^l \rho I\phi_m'\phi_n'\,\mathrm{d}x\ddot{a}_m + 2\Omega\int_0^l \rho I\phi_m'\phi_n'\,\mathrm{d}x\dot{b}_m + \int_0^l EI\phi_m''\phi_n''\,\mathrm{d}x a_m\right\} = P_v\phi_n,$$
$$n = 1,2,\ldots,N_p, \tag{8}$$

$$\sum_{n=1}^{N_p}\left\{\int_0^l \rho A\phi_m\phi_n\,\mathrm{d}x\ddot{b}_n + \int_0^l \rho I\phi_m'\phi_n'\,\mathrm{d}x\ddot{b}_n - 2\Omega\int_0^l \rho I\phi_m'\phi_n'\,\mathrm{d}x\dot{a}_n + \int_0^l EI\phi_m''\phi_n''\,\mathrm{d}x b_n\right\} = P_w\phi_m,$$
$$m = 1,2,\ldots,N_p. \tag{9}$$

Combining Eqs. (8) and (9), the equations of motion can be arranged as the matrix form

$$\begin{bmatrix}[\mathbf{M_T}]+[\mathbf{M_R}] & 0\\ 0 & [\mathbf{M_T}]+[\mathbf{M_R}]\end{bmatrix}\begin{Bmatrix}\ddot{\underline{\mathbf{a}}}\\ \ddot{\underline{\mathbf{b}}}\end{Bmatrix} + 2\Omega\begin{bmatrix}0 & [\mathbf{M_R}]\\ -[\mathbf{M_R}] & 0\end{bmatrix}\begin{Bmatrix}\dot{\underline{\mathbf{a}}}\\ \dot{\underline{\mathbf{b}}}\end{Bmatrix} + \begin{bmatrix}[\mathbf{K_S}] & 0\\ 0 & [\mathbf{K_S}]\end{bmatrix}\begin{Bmatrix}\underline{\mathbf{a}}\\ \underline{\mathbf{b}}\end{Bmatrix} = \begin{Bmatrix}\underline{\mathbf{R}}_{\mathbf{a}}\\ \underline{\mathbf{R}}_{\mathbf{b}}\end{Bmatrix}, \tag{10}$$

where the state vectors $\underline{\mathbf{a}}$ and $\underline{\mathbf{b}}$ are defined as $\underline{\mathbf{a}}^{\mathrm{T}} = [a_1, a_2, \ldots, a_{N_p}]$ and $\underline{\mathbf{b}}^{\mathrm{T}} = [b_1, b_2, \ldots, b_{N_p}]$, respectively. The elements of these matrices $[\mathbf{M_T}]$, $[\mathbf{M_R}]$, and $[\mathbf{K_S}]$ can be expressed as

$$\mathbf{M_T}(m,n) = \int_0^l \rho A\phi_m\phi_n\,\mathrm{d}x,$$

$$\mathbf{M_R}(m,n) = \int_0^l \rho I\phi_m'\phi_n'\,\mathrm{d}x,$$

$$\mathbf{K_S}(m,n) = \int_0^l EI\phi_m''\phi_n''\,\mathrm{d}x. \tag{11}$$

In addition, the force vectors $\{\underline{\mathbf{R}}_{\mathbf{a}}\}$ and $\{\underline{\mathbf{R}}_{\mathbf{b}}\}$ are of the forms

$$\underline{\mathbf{R}}_{\mathbf{a}}^{\mathrm{T}} = P_v[\phi_1, \phi_2, \ldots, \phi_n],$$

$$\underline{\mathbf{R}}_{\mathbf{b}}^{\mathrm{T}} = P_w[\phi_1, \phi_2, \ldots, \phi_m]. \tag{12}$$

It is noted that the generalized mass matrices $[\mathbf{M_T}]$ and $[\mathbf{M_R}]$ are formulated from the kinetic energy of the flexible shaft, which correspond to the contribution of translational inertia and rotary inertia, respectively. The matrix $[\mathbf{M_R}]$ related to the generalized velocity multiplied by 2Ω is due to the gyroscopic effect. The generalized stiffness matrix $[\mathbf{K_S}]$ is derived from the contribution of bending strain energy of the shaft. For simplicity, Eq. (10) can be expressed as

$$[\mathbf{M}]\ddot{\underline{\mathbf{q}}} + [\mathbf{C}]\dot{\underline{\mathbf{q}}} + [\mathbf{K}]\underline{\mathbf{q}} = \{\mathbf{F}\}, \tag{13}$$

where $\underline{\mathbf{q}}^{\mathrm{T}} = [\underline{\mathbf{a}}^{\mathrm{T}}, \underline{\mathbf{b}}^{\mathrm{T}}]$.

3. The transformation matrix for geometric constraints

Fig. 2 shows the configurations of a multi-span shaft with general boundary conditions such as hinged–hinged (h–h), clamped–hinged (c–h) and clamped–clamped (c–c) conditions. It should be noted that

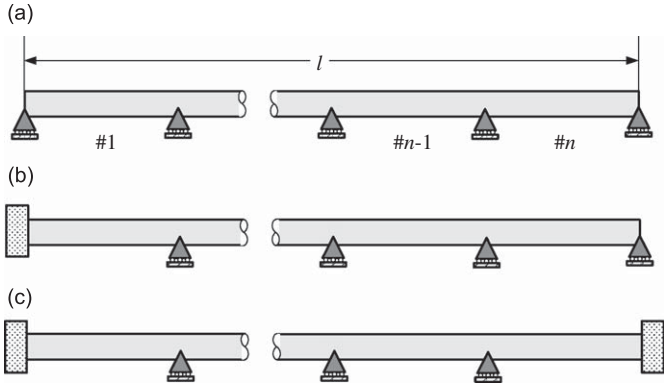

Fig. 2. The configurations of an equidistance multi-span shaft with (a) h–h, (b) c–h, and (c) c–c conditions.

the shaft does not satisfy the geometric constraints since the mode shape functions are arbitrary functions. Therefore, the present study proposes a modified transformation matrix to deal with the multi-span geometric constraints including the boundaries and intermediate supports. Since the geometric conditions in Y and Z directions are isotropic, only the constraint equations related to the deflection V are derived.

The geometric constraints of the hinged support and clamped support can be expressed as follows:

$$V(x_i^h, t) = 0, \quad i = 1, 2, \ldots, n_h, \tag{14}$$

$$V(x_j^c, t) = 0, \quad V'(x_j^c, t) = 0, \quad j = 1, 2, \ldots, n_c, \tag{15}$$

where x_i^h and x_j^c denote the axial positions of the i-th hinged support and j-th clamped support, respectively, and n_h and n_c are the numbers of hinged supports and clamped supports, respectively. In Eq. (15), it shows the displacements at the clamped supports of the shaft and the corresponding slopes are zeros. Substituting Eqs. (14) and (15) into Eq. (3), the geometric constraint equations for hinged supports and clamped supports can be expressed as Eqs. (16) and (17), respectively,

$$\begin{bmatrix} 1 & (x_1^h) & \cdots & (x_1^h)^{N_p-1} \\ 1 & (x_2^h) & \cdots & (x_2^h)^{N_p-1} \\ & & \vdots & \\ 1 & (x_{n_h}^h) & \cdots & (x_{n_h}^h)^{N_p-1} \end{bmatrix} \begin{Bmatrix} a_1 \\ a_2 \\ \vdots \\ a_{N_p} \end{Bmatrix} = 0, \tag{16}$$

$$\begin{bmatrix} 1 & x_1^c & (x_1^c)^2 & \cdots & (x_1^c)^{N_p-1} \\ & & \vdots & \cdots & \\ 1 & x_{n_c}^c & (x_{n_c}^c)^2 & \cdots & (x_{n_c}^c)^{N_p-1} \\ 0 & 1 & 2x_1^c & \cdots & (N_p-1)(x_1^c)^{N_p-2} \\ & & \vdots & \cdots & \\ 0 & 1 & 2x_{n_c}^c & \cdots & (N_p-1)(x_{n_c}^c)^{N_p-2} \end{bmatrix} \begin{Bmatrix} a_1 \\ a_2 \\ a_3 \\ \vdots \\ a_{N_p} \end{Bmatrix} = 0. \tag{17}$$

Combining Eqs. (16) and (17), the first $k = n_h + 2n_c$ generalized coordinates can be written as

$$\begin{Bmatrix} a_1 \\ a_2 \\ \vdots \\ a_k \end{Bmatrix} = \begin{bmatrix} [\mathbf{R_h}] \\ [\mathbf{R_c}] \end{bmatrix} \underline{\mathbf{a}}_\mathbf{I} = [\mathbf{R_{hc}}] \underline{\mathbf{a}}_\mathbf{I}, \tag{18}$$

where $\underline{\mathbf{a}}_\mathbf{I}^{\mathrm{T}} = \{a_{k+1}, a_{k+2}, \ldots, a_{N_p}\}$ and the matrices $[\mathbf{R_h}]$ and $[\mathbf{R_c}]$ are of the forms

$$[\mathbf{R_h}] = -\begin{bmatrix} 1 & x_1^h & \cdots & (x_1^h)^{k-1} \\ 1 & x_2^h & \cdots & (x_2^h)^{k-1} \\ & & \vdots & \\ 1 & x_{n_h}^h & \cdots & (x_{n_h}^h)^{k-1} \end{bmatrix}^{-1} \begin{bmatrix} (x_1^h)^k & (x_1^h)^{k+1} & \cdots & (x_1^h)^{N_p-1} \\ (x_2^h)^k & (x_2^h)^{k+1} & \cdots & (x_2^h)^{N_p-1} \\ & & \vdots & \\ (x_{n_h}^h)^k & (x_{n_h}^h)^{k+1} & \cdots & (x_{n_h}^h)^{N_p-1} \end{bmatrix}, \tag{19}$$

$$[\mathbf{R_c}] = -\begin{bmatrix} 1 & x_1^c & (x_1^c)^2 & \cdots & (x_1^c)^{k-1} \\ & & \vdots & & \\ 1 & x_{n_c}^c & (x_{n_c}^c)^2 & \cdots & (x_{n_c}^c)^{k-1} \\ 0 & 1 & 2x_1^c & \cdots & (k-1)(x_1^c)^{k-2} \\ & & \vdots & & \\ 0 & 1 & 2x_{n_c}^c & \cdots & (k-1)(x_{n_c}^c)^{k-2} \end{bmatrix}^{-1} \begin{bmatrix} (x_1^c)^k & (x_1^c)^{k+1} & \cdots & (x_1^c)^{N_p-1} \\ & & \vdots & \\ (x_{n_c}^c)^k & (x_{n_c}^c)^{k+1} & \cdots & (x_{n_c}^c)^{N_p-1} \\ (k)(x_1^c)^{k-1} & (k+1)(x_1^c)^k & \cdots & (N_p-1)(x_1^c)^{N_p-2} \\ & & \vdots & \\ (k)(x_{n_c}^c)^{k-1} & (k+1)(x_{n_c}^c)^k & \cdots & (N_p-1)(x_{n_c}^c)^{N_p-2} \end{bmatrix}. \tag{20}$$

The dimensions of the matrices $[\mathbf{R_h}]$ and $[\mathbf{R_c}]$ are $n_h \times (N_p - k)$ and $2n_c \times (N_p - k)$, respectively. If the hinged supports or clamped supports exist alone, only the corresponding matrix $[\mathbf{R_h}]$ or $[\mathbf{R_c}]$ in Eq. (18) is considered. The first k elements of state vector $\boldsymbol{a}$ in Eq. (10) are substituted by Eq. (18), and the state vector $\underline{\mathbf{a}}$ can be rearranged as

$$\underline{\mathbf{a}} = [\mathbf{R_{hc}^a}]\underline{\mathbf{a}}_\mathbf{I} = \begin{bmatrix} [\mathbf{R_{hc}}] \\ [\mathbf{I}] \end{bmatrix} \underline{\mathbf{a}}_\mathbf{I}, \tag{21}$$

where $[\mathbf{R_{hc}^a}]$ is the constraint matrix satisfying the geometric constraints of both the hinged supports and clamped supports in Y direction and $[\mathbf{I}]$ is the unit matrix. Similarly, the constraint matrix $[\mathbf{R_{hc}^b}]$ satisfying the geometric constraints in Z direction and related to the vector $\underline{\mathbf{b}}_\mathbf{I}^{\mathrm{T}} = \{b_{k+1}, b_{k+2}, \ldots, b_{N_p}\}$ can be obtained through the same procedures. Denoting $\underline{\mathbf{q}}_\mathbf{I}^{\mathrm{T}} = [\underline{\mathbf{a}}_\mathbf{I}^{\mathrm{T}}, \underline{\mathbf{b}}_\mathbf{I}^{\mathrm{T}}]$, the system generalized coordinate vector $\underline{\mathbf{q}}$ in Eq. (13) can be rewritten as

$$\underline{\mathbf{q}} = [\mathbf{R_T}]\underline{\mathbf{q}}_\mathbf{I} = \begin{bmatrix} [\mathbf{R_{hc}^a}] & [\mathbf{0}] \\ [\mathbf{0}] & [\mathbf{R_{hc}^b}] \end{bmatrix} \underline{\mathbf{q}}_\mathbf{I}, \tag{22}$$

where $[\mathbf{R_T}]$ represents the transformation matrix for the multi-span geometric constraints. Substituting Eq. (22) into Eq. (13) to obtain the substituted equation, then premultiplying the transpose of matrix $[\mathbf{R_T}]$ with the substituted equation, finally the system equations of motion with associated geometric constraints can be represented as

$$[\mathbf{R_T}]^{\mathrm{T}}[\mathbf{M}][\mathbf{R_T}]\ddot{\underline{\mathbf{q}}}_\mathbf{I} + [\mathbf{R_T}]^{\mathrm{T}}[\mathbf{C}][\mathbf{R_T}]\dot{\underline{\mathbf{q}}}_\mathbf{I} + [\mathbf{R_T}]^{\mathrm{T}}[\mathbf{K}][\mathbf{R_T}]\underline{\mathbf{q}}_\mathbf{I} = [\mathbf{R_T}]^{\mathrm{T}}\{\mathbf{F}\}. \tag{23}$$

4. Results and discussions

The dynamic response of a rotating multi-span shaft with general boundary conditions and subjected to a constant moving load is investigated. Here P_v is assumed to be zero, and only the load $P_w = EId_0/l^3$ acts on the shaft. Therefore, the deflection induced by the gyroscopic effect can be isolated [1–4,7,15]. The material properties and geometric dimensions of the shaft are given as: density $\rho = 7700\,\mathrm{kg\,m^{-3}}$, elastic modulus $E = 2.07 \times 10^{11}\,\mathrm{Pa}$, length $l = 1.0\,\mathrm{m}$, and diameter $d_0 = 4\beta l/\pi$, where β is the Rayleigh beam coefficient and $\beta = 0.03$ is taken in this study. The Euler–Bernoulli beam is realized if β is close to zero. The nondimensional parameters of moving speed and rotational speed are denoted by $\alpha = \pi v/l\omega_0$ and $\overline{\Omega} = \Omega/\omega_0$, respectively,

where $\omega_0 = (\pi/l)^2\sqrt{EI/\rho A}$ is the fundamental natural frequency of simply supported Euler–Bernoulli beam. The equations of motion in Eq. (23) are solved by the Runge–Kutta method to obtain dynamic response. The initial values are chosen as zeros. The following nondimensional parameters are defined to illustrate the numerical results: $\overline{s} = x/l$ represents the position of moving load; $\overline{V} = V/V_s$ and $\overline{W} = W/W_s$ represent the deflection at $\overline{s}$ in Y and Z directions, respectively, where $V_s = W_s = P_w l^3/48EI$ is the static deflection of the stationary simply supported shaft subjected to the same load at the midpoint; $\overline{V}_m$ and $\overline{W}_m$ denote the maximum deflection at $\overline{s}$ in Y and Z directions, respectively, and the associated occurring positions denote $\overline{s}_v$ and $\overline{s}_w$, respectively. The effects of moving speed, rotational speed, and number of spans on the dynamic response are discussed. The ranges of moving speed and rotational speed considered in this study are $0<\alpha\leqslant 3$ and $0<\overline{\Omega}\leqslant 2.5$, respectively. Moreover, the lengths of spans are assumed to be equal and the one to three-span shafts are considered.

4.1. Comparison of natural frequencies using GAMM and FEM

A comparison of natural frequencies obtained by both the present method and FEM is given to ensure the accuracy of numerical results. The natural frequencies can be obtained by solving the eigenvalues problem of Eq. (23). The dimension of the matrix of eigenvalues problem (DMEP) depends on the numbers of mode shape functions N_p, clamped supports n_c, and hinged supports n_h, and it can be obtained by the formula $\mathrm{DMEP} = N_p - 2n_c - n_h$. Tables 1–3 show the first five natural frequencies using the present method with

Table 1
The natural frequencies of shaft with the h–h case ($n_c = 0$) obtained by GAMM|FEM (shown in bold).

	Single-span ($n_h = 2$)	Two-span ($n_h = 3$)	Three-span ($n_h = 4$)
1	77.7|**77.7**| 77.7	310.5|**310.6**	697.1|**697.7**
2	310.5|**310.6**| 310.5	488.8|**485.3**	901.5|**894.3**
3	697.3|**698.0**| 697.1	1237.2|**1240.4**	1378.4|**1306.9**
4	1237.2|**1240.4**| 1235.5	1623.8|**1572.5**	2782.1|**2788.1**
5	2078.7|**1940.6**| 1922.8	3125.8|**2805.8**	3902.3|**3185.1**

Note: Results marked by underline are exact solutions; Unit: Hz.

Table 2
The natural frequencies of shaft with the c–h case ($n_c = 1$) obtained by GAMM|FEM (shown in bold).

	Single-span ($n_h = 1$)	Two-span ($n_h = 2$)	Three-span ($n_h = 3$)
1	121.4|**121.4**	362.7|**362.4**	752.2|**751.6**
2	393.0|**393.1**	631.5|**627.2**	1098.0|**1090.5**
3	818.0|**819.4**	1348.2|**1346.9**	1517.2|**1499.4**
4	1398|**1401.3**	1877.4|**1816.3**	2924.5|**2903.9**
5	2145.4|**2142.6**	3027.7|**2967.7**	3764.2|**3543.0**

Unit: Hz.

Table 3
The natural frequencies of shaft with the c–c case ($n_c = 2$) obtained by GAMM|FEM (shown in bold).

	Single-span ($n_h = 0$)	Two-span ($n_h = 1$)	Three-span ($n_h = 2$)
1	176.2|**176.2**	485.0|**485.3**	894.4|**894.3**
2	485.0|**485.3**	707.9|**704.6**	1312.1|**1306.9**
3	948.5|**950.7**	1562.9|**1572.5**	1607.3|**1585.2**
4	1562.9|**1572.5**	1969.9|**1945.6**	3184.3|**3185.1**
5	2361.3|**2355.1**	3332.8|**3303.1**	4073.7|**3918.7**

Unit: Hz.

DMEP = 8 and FEM with eight elements for various boundary conditions. The percentage differences $|(\omega_{n,\mathrm{GAMM}}-\omega_{n,\mathrm{FEM}})/\omega_{n,\mathrm{FEM}}|$ of the first four natural frequencies do not exceed 5 percent for all boundary cases. It should be noted that the numerical results using GAMM for the single-span shaft with the h–h case are in good agreement with exact solutions. Nevertheless, the percentage differences of the 5th natural frequencies of the h–h, c–h, and c–c cases for the single-span shaft are 7.1, 0.13, and 0.2 percent, respectively, as for the two-span shaft are 11.4, 2, 0.9 percent, and as for the three-span shaft are 22.5, 6.2, and 3.9 percent. The percentage differences of the h–h and c–h cases are larger than those of the c–c case, especially for the three-span shaft. This is because the zero moment at the hinged boundary is not constrained, as expressed in Eq. (14). However, the convergent performance of the natural frequencies can be improved through the increase of DMEP. In addition, the numerical results show that the lower natural frequencies are the first to be converged by using GAMM.

4.2. Convergence test for dynamic response

The convergence test with respect to DMEP is based on maximum deflections. Tables 4–6 show the value of $\overline{W}_m$ at $\alpha = 0.5$ and $\overline{\Omega} = 2.5$ for different boundary cases. The percentage differences defined by $|(\overline{W}_{m,\mathrm{DMEP}=n} - \overline{W}_{m,\mathrm{DMEP}=10})/\overline{W}_{m,\mathrm{DMEP}=10}|$ of the maximum deflections with DMEP = 6 and 8 are compared. As DMEP = 6, the percentage differences for the three-span shaft of the h–h, c–h and c–c cases are 3.8, 1.7 and 10.16 percent, respectively, which are all larger than those of single and two-span shafts. However, the percentage difference for the three-span shaft with the c–c case is significantly reduced to 2.1 percent when DMEP is increased to 8. And the percentage differences for other boundary cases are all smaller than 0.6 percent. The numerical results of the single-span shaft with the h–h case obtained by the present method are in very good agreement with the solution from Katz et al. [1]. Notably, the convergent performance for the

Table 4
Convergence test with respect to DMEP for the value of $\overline{W}_m$ of the h–h case ($n_c = 0$) at $\alpha = 0.5$ and $\overline{\Omega} = 2.5$.

DMEP	Single-span ($n_h = 2$)	Two-span ($n_h = 3$)	Three-span ($n_h = 4$)
6	1.5933	0.1060	0.02699
8	1.5958	0.1085	0.02788
10	1.5962	0.1091	0.02808
Katz [1]	1.597	–	–

Table 5
Convergence test with respect to DMEP for the value of $\overline{W}_m$ of the c–h case ($n_c = 1$) at $\alpha = 0.5$ and $\overline{\Omega} = 2.5$.

DMEP	Single-span ($n_h = 1$)	Two-span ($n_h = 2$)	Three-span ($n_h = 3$)
6	0.7373	0.0962	0.0280
8	0.7383	0.0959	0.0281
10	0.7387	0.0961	0.0286

Table 6
Convergence test with respect to DMEP for the value of $\overline{W}_m$ of the c–c case ($n_c = 2$) at $\alpha = 0.5$ and $\overline{\Omega} = 2.5$.

DMEP	Single-span ($n_h = 0$)	Two-span ($n_h = 1$)	Three-Span ($n_h = 2$)
6	0.2967	0.0461	0.0168
8	0.2977	0.0463	0.0183
10	0.2980	0.0465	0.0187

natural frequencies of the c–c case is indicated to be better than other boundary cases from the previous comparison of natural frequencies. However, the convergent performance for dynamic responses of the c–c case is not the best. This can be explained that the actual mode shapes of a rotating shaft with the c–c case are quite different from the mode shape functions chosen by GAMM. Nevertheless, according to the results of the convergence rest for dynamic responses and the comparison of natural frequencies using FEM, the numerical results can be accurately obtained when DMEP = 8.

4.3. Analysis of dynamic response

The numerical results are obtained using DMEP = 8 based on the previous result of convergence test. Fig. 3 shows the correlations of the α vs. $\overline{W}_m$ and α vs. $\overline{V}_m$ for the single-span shaft at $\overline{\Omega} = 2.5$ and the associated correlations of the α vs. $\bar{s}_w$ and α vs. $\bar{s}_v$. The value of $\overline{W}_m$ is the largest for the h–h case, while the c–c case exhibits the smallest value, as shown in Fig. 3(a). However, the difference will be small with increase of α. Furthermore, the maximum values of $\overline{W}_m$ for the h–h, c–h and c–c cases are 1.604 at $\alpha = 0.45$, 0.7608 at $\alpha = 0.6$, and 0.383 at $\alpha = 0.84$, respectively. The results show that the clamped support can increase the system stiffness and cause the maximum value of $\overline{W}_m$ to occur at the large value of α. Fig. 3(b) indicates that the maximum deflection occurs near the midpoint of the shaft in the range $0 < \alpha \leqslant 0.39$ for each boundary case. As $0.39 < \alpha \leqslant 3$, the maximum deflection gradually moves to the left end of shaft with increase of α, especially for the h–h case due to the zero moments at the hinged supports. However, the maximum deflections of the c–h and c–c cases almost occur at the same position for varying values of α. Fig. 3(c) shows that the value of $\overline{V}_m$ is approximately three order of magnitude smaller than that of $\overline{W}_m$. And the deflection in Y direction is induced by the gyroscopic effect. The value of α corresponding to the maximum value of $\overline{V}_m$ does not match with that of $\overline{W}_m$ for each boundary case, but the distribution curve is similar to that of $\overline{W}_m$. The correlation of α vs. $\bar{s}_v$ shown in Fig. 3(d) presents the piecewise continuous distributions. The value of $\bar{s}_v$ in each piecewise distribution will decrease as α increases, and it is always smaller than 0.5. This implies that the maximum deflection in Y direction always occurs toward the left end of shaft, especially for the larger value of α. Fig. 4

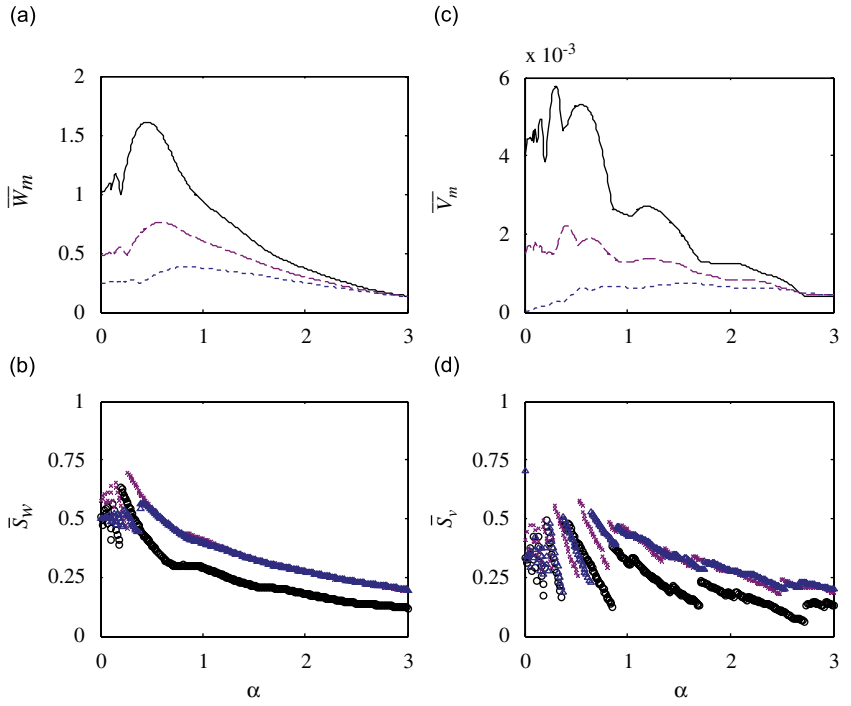

Fig. 3. The correlations of (a) α vs. $\overline{W}_m$, (b) α vs. $\bar{s}_w$, (c) α vs. $\overline{V}_m$, and (d) α vs. $\bar{s}_v$ for the single-span shaft at $\overline{\Omega} = 2.5$. ——, ◦, h–h case; - - - -, ×, c–h case; · · · · · · · , Δ, c–c case.

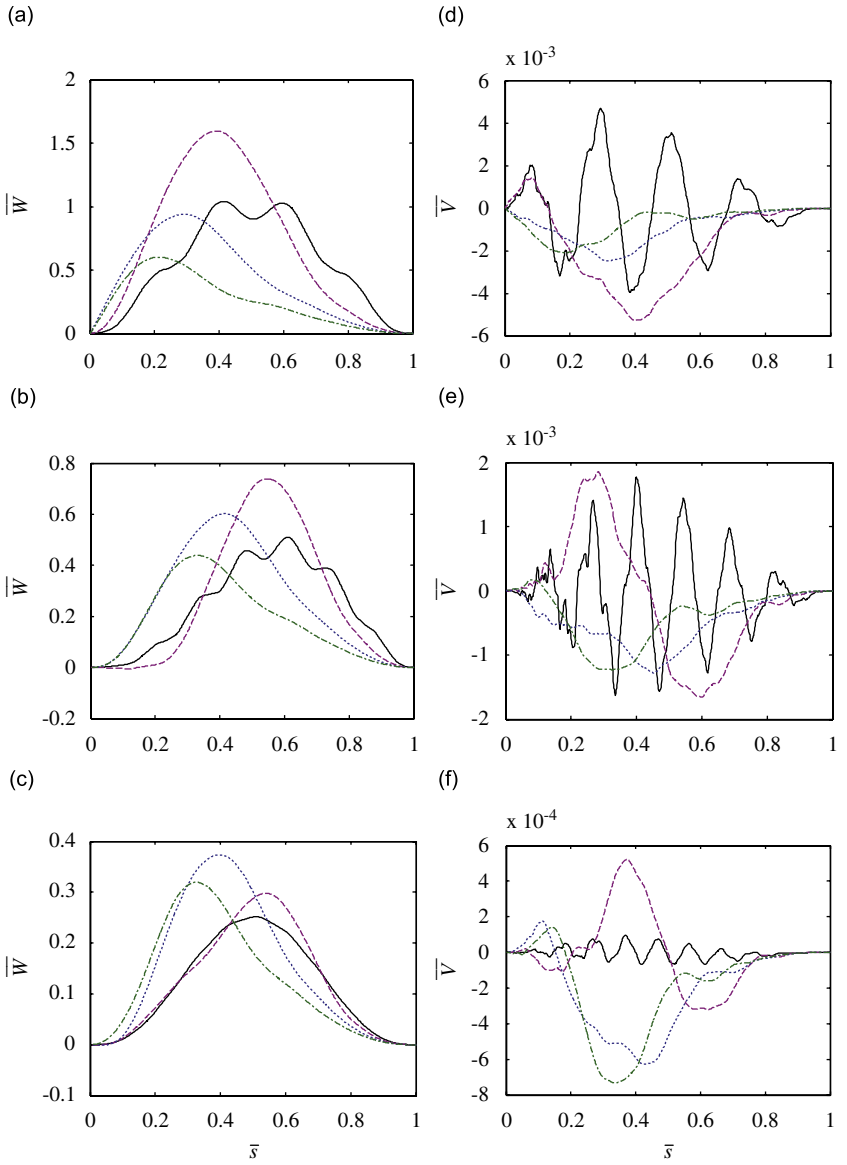

Fig. 4. The deflections under the moving load in Z direction for (a) h–h, (b) c–h, and (c) c–c cases as well as in Y direction for (d) h–h, (e) c–h, and (f) c–c cases for the single-span shaft at $\overline{\Omega} = 2.5$. ——, $\alpha = 0.11$; ----, $\alpha = 0.5$; · · · · · · · ·, $\alpha = 1.0$; ——, $\alpha = 1.5$.

shows the deflections of shaft under the moving load in Y and Z directions for the single-span shaft at $\alpha = 0.11$, 0.5, 1.0 and 1.5. The deflection curve with $\alpha = 0.11$ exhibits several undulations for the h–h and c–h cases, while the c–c case presents the smooth deflection curve, as shown in Figs. 4(a)–(c). This phenomenon can be explained that the original deformation of the entire shaft have enough time for completely changing into another one before the next time step. Thus that may cause the additional increment or decrement in the deflection of the shaft at the following loading position. This phenomenon for the h–h and c–h cases occurs, respectively, in the ranges $0 < \alpha \leqslant 0.2$ and $0 < \alpha \leqslant 0.26$, as the regions with minor fluctuations shown in Fig. 3(a). Within the ranges, the number of undulations will decrease for the larger value of α, but the amplitude of undulation will become larger. If the value of α exceeds the ranges, the shape of the deflection curve will gradually develop a single smooth hump. The deflection curve with $\alpha = 0.11$ in Y direction is clearly indicated from Figs. 4(d)–(f) to oscillate along the longitudinal axis, especially for the c–c case. In addition, the

oscillation frequency along the longitudinal axis will increase as α decrease, but the amplitude of the oscillation will decline.

Figs. 5(a) and (b) present the correlation of α vs. $\overline{W}_m$ for two-span shaft at $\overline{\Omega}=2.5$ and the associated correlation of α vs. $\overline{s}_w$. The deflection of shaft can be significantly reduced by adding an intermediate support, as observed from a comparison with Figs. 5(a) and 3(a). The maximum values of $\overline{W}_m$ for the h–h, c–h and c–c cases are 0.254 at $\alpha=1.5$, 0.131 at $\alpha=1.71$, and 0.12 at $\alpha=1.95$, respectively, and the corresponding occurring positions are all at the first span. The difference between the values of $\overline{W}_m$ for the h–h and c–h cases are not significant in the two ranges $0<\alpha\leqslant 1.03$ and $2.38<\alpha\leqslant 3$. The value of $\overline{V}_m$ is observed from Fig. 5(c) to be always the largest for the h–h case, while the c–c case presents the smallest value. Fig. 5(d) indicates that the maximum deflection in Y direction always appears at the first span, and it will be closer to the left end of the span as the value of α increases. Generally, when the slope of the distribution curve of α vs. $\overline{V}_m$ is not continuous, the distribution of $\overline{s}_v$ will have a jump discontinuity at the corresponding value of α. Also, this phenomenon exists in the correlations of α vs. $\overline{W}_m$ and α vs. $\overline{s}_w$. Fig. 6 presents the deflections of shaft under the moving load in Y and Z directions for the two-span shaft. The deflection curves with $\alpha=0.11$ and 0.5 present several undulations for the h–h and c–h cases, as shown in Figs. 6(a) and (b). The phenomenon occurs in the ranges of $0<\alpha\leqslant 0.6$ for the h–h case and $0<\alpha\leqslant 0.5$ for the c–h case, respectively. It should be noted that the shaft deflects in a direction opposite to the load near the junction between two adjacent spans, especially for the h–h case with large value of α. For instance in the h–h case with $\alpha=1.5$, the negative deflection exists in the range $\overline{s}=0.37-0.5$ and the minimum value is about -0.023 at $\overline{s}=0.43$. This is because the shaft does not have enough time to recover from the previous deformation before the next time step. The phenomenon can be illustrated from the varying deformations of the entire shaft shown in Fig. 7 while the load rapidly traverses through the junction.

Fig. 8 displays the correlations of α vs. $\overline{W}_m$ and α vs. $\overline{V}_m$ or the three-span shaft at $\overline{\Omega}=2.5$ and the associated correlations of α vs. $\overline{s}_w$ and α vs. $\overline{s}_v$. Fig. 8(a) shows that the values of α corresponding to the maximum values of $\overline{W}_m$ for the h–h, c–h, and c–c cases are 2.4, 2.25 and 3.0, respectively, and they are larger then those of the two-span shaft. The difference between the values of $\overline{W}_m$ of the h–h and c–h cases is not

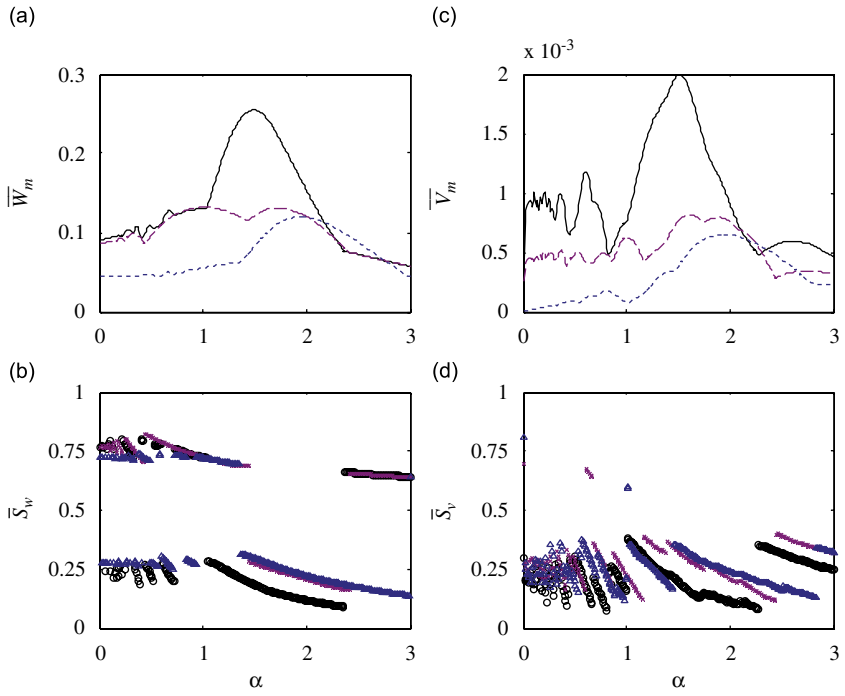

Fig. 5. The correlations of (a) α vs. $\overline{W}_m$, (b) α vs. $\overline{s}_w$, (c) α vs. $\overline{V}_m$, and (d) α vs. $\overline{s}_v$ for the two-span shaft at $\overline{\Omega}=2.5$. —— ◦, h–h case; - - - -, ×, c–h case; · · · · · · · , Δ, c–c case.

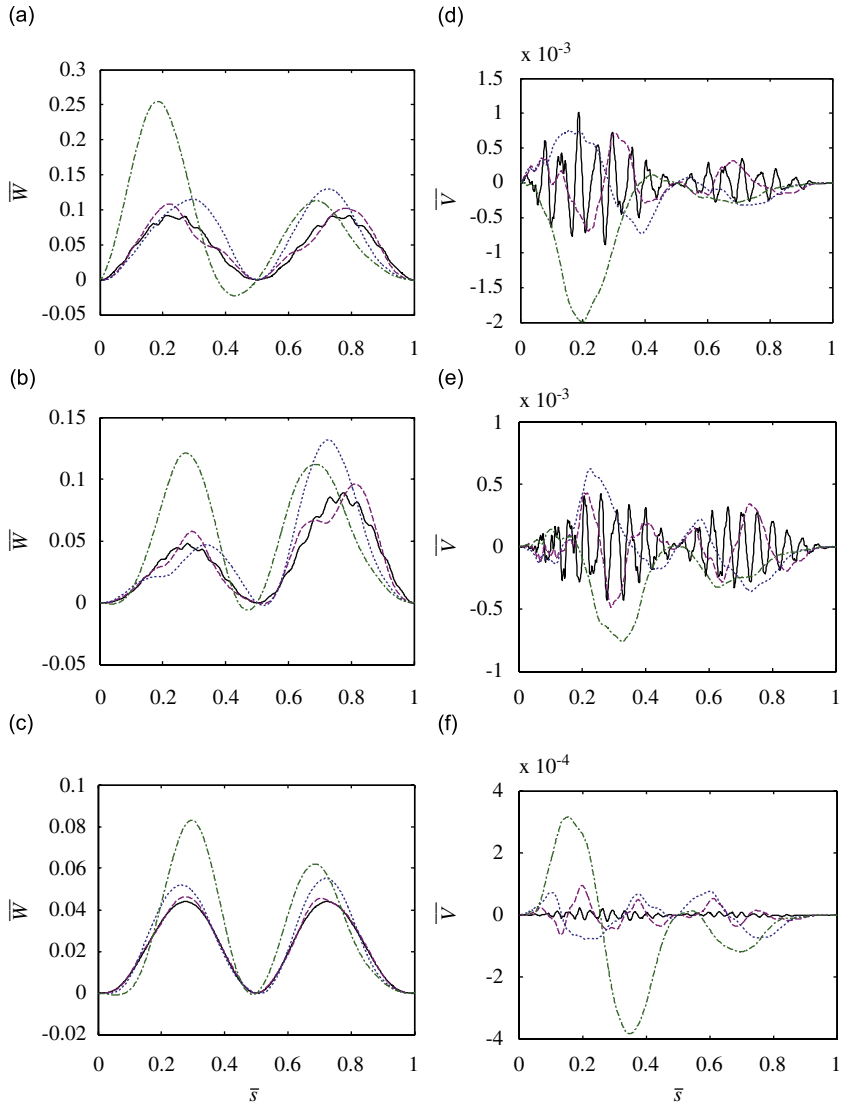

Fig. 6. The deflections under the moving load in Z direction for (a) h–h, (b) c–h, and (c) c–c cases as well as in Y direction for (d) h–h, (e) c–h, and (f) c–c cases for the two-span shaft at $\overline{\Omega} = 2.5$, ——, $\alpha = 0.11$; ----, $\alpha = 0.5$; · · · · · · · , $\alpha = 1.0$; ——, $\alpha = 1.5$.

significant in the range $0 < \alpha \leqslant 1.74$. And this range is wider than that of the two-span shaft. Fig. 8(b) shows that the maximum deflection is closer to the midpoint of one span in comparison with the two-span shaft. Fig. 8(c) indicates that the maximum deflection in Y direction for the h–h case is always larger than that for the c–h and c–c cases. However, the maximum deflection does not occur at the third span for each boundary case, as shown in Fig. 8(d). Fig. 9 demonstrates the deflections of shaft under the moving load in Y and Z directions for the three-span shaft. The peak deflections of the three-span shaft are closer to the midpoints of each span than in the two-span shaft, as shown in Figs. 9(a)–(c). Notably, the maximum deflections of the h–h and c–h cases are not significantly different. This result can also be reaffirmed by Fig. 8(a) in the range $0 < \alpha \leqslant 1.74$. Moreover, the deflection curves with $\alpha = 0.11$ and 0.5 shown in Figs. 9(a) and (b) contain several undulations. In fact, this phenomenon occurs when $\alpha \leqslant 0.83$ for the h–h case and $\alpha \leqslant 0.63$ for the c–h case. Those ranges for the three-span shaft are wider than those of the two-span shaft. Within these ranges, the associated correlation of α vs. $\overline{s}_w$ always presents piecewise continuous distributions. The value of $\overline{V}$ is indicated from Figs. 9(d)–(f) to be significantly reduced due to the intermediate supports. However, the

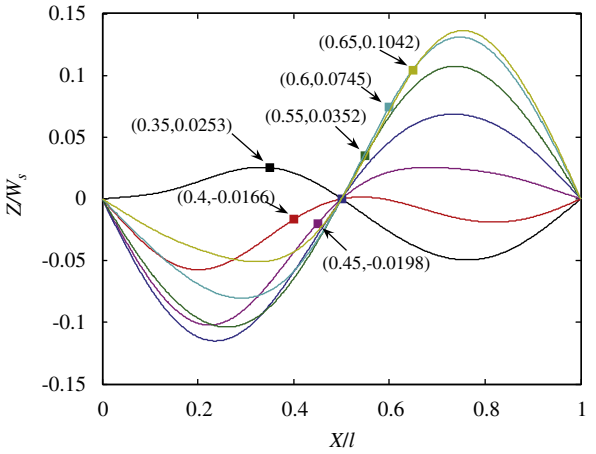

Fig. 7. The instantaneous deformations of the entire shaft in Z direction for the two-span shaft with the h–h case at $\alpha = 1.5$ and $\overline{\Omega} = 2.5$ versus varying positions of the moving load.

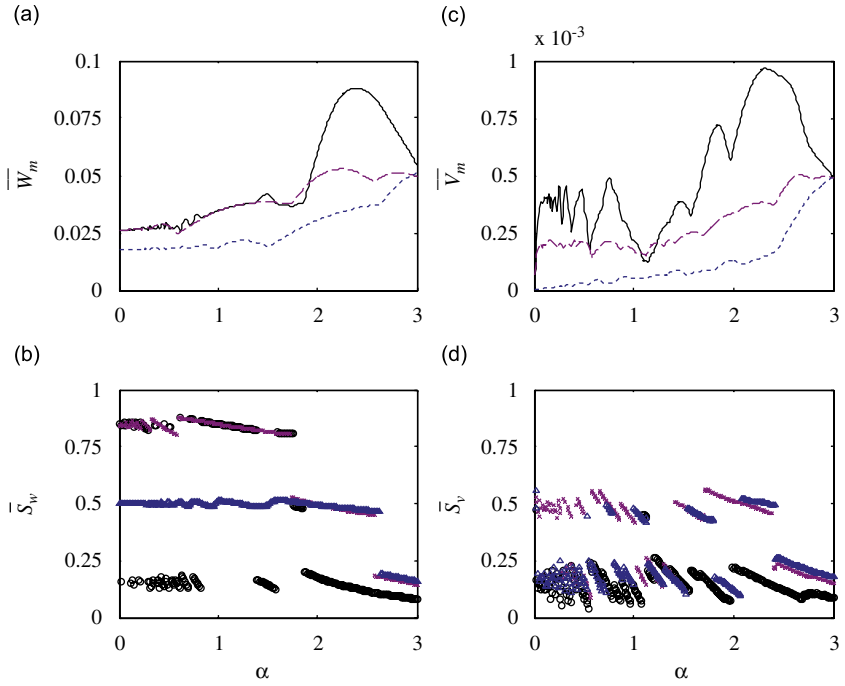

Fig. 8. The correlations of (a) α vs. $\overline{W}_m$, (b) α vs. $\bar{s}_w$, (c) α vs. $\overline{V}_m$, and (d) α vs. $\bar{s}_v$ for the three-span shaft at $\overline{\Omega} = 2.5$. ——, ◦, h–h case; - - - -, ×, c–h case; · · · · · · · , Δ, c–c case.

deflection curve obviously oscillates along the longitude axis, and the oscillation frequency also increases for all boundary cases in comparison with the single and two-span shafts.

The above numerical results are obtained at $\overline{\Omega} = 2.5$. If the rotational speed is decreased to $\overline{\Omega} = 0.5$, only the deflection induced by the gyroscopic effect in Y direction is significantly affected, as indicated in Table 7 for the three-span shaft with the h–h case. The deflection of the shaft is directly proportional to the rotational speed. Nevertheless, the positions of maximum deflections on the shaft do not vary in both the Y and Z directions.

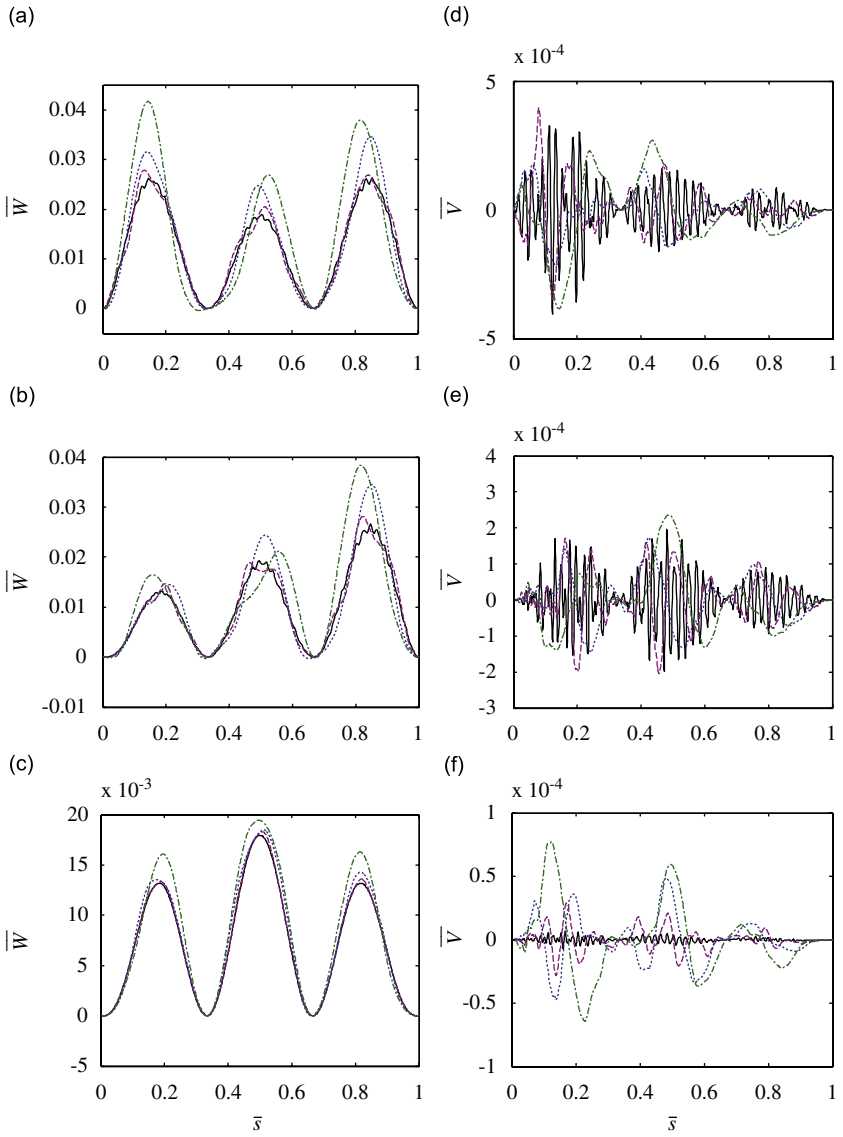

Fig. 9. The deflections under the moving load in Z direction for (a) h–h, (b) c–h, and (c) c–c cases as well as in Y direction for (d) h–h, (e) c–h, and (f) c–c cases for the three-span shaft at $\overline{\Omega} = 2.5$. ——, $\alpha = 0.11$; ----, $\alpha = 0.5$; · · · · · · · ·, $\alpha = 1.0$; ——, $\alpha = 1.5$.

Table 7
The maximum deflections and the corresponding deflecting positions in Y and Z directions for three-span shaft at $\overline{\Omega} = 0.5$ and 2.5.

α	$\overline{\Omega} = 0.5$				$\overline{\Omega} = 2.5$			
	$\overline{V}_m$	$\overline{s}_v$	$\overline{W}_m$	$\overline{s}_w$	$\overline{V}_m$	$\overline{s}_v$	$\overline{W}_m$	$\overline{s}_w$
0.11	8.267E−5	0.122	2.626E−2	0.854	4.050E−4	0.122	2.626E−2	0.854
0.5	7.999E−5	0.080	2.790E−2	0.130	3.963E−4	0.080	2.788E−2	0.130
1.0	4.391E−5	0.134	3.459E−2	0.849	2.189E−4	0.134	3.459E−2	0.849
1.5	7.680E−5	0.144	4.168E−2	0.142	3.835E−4	0.144	4.167E−2	0.142

5. Conclusions

The dynamic response of a rotating multi-span shaft with general boundary conditions subjected to a moving load is studied. A modified transformation matrix based on GAMM is proposed to dealing with the multi-span geometric constraints. The proposed method has the merits of accuracy and efficiency compared to FEM. The effects of the parameters of moving speed α, rotational speed $\overline{\Omega}$ and number of spans on the deflections under the moving load are presented for the cases of the h–h, c–h and c–c. In addition, the effects on the occurring position of maximum deflection are discussed. The numerical results can be summarized as follows:

1. The deflections in both the Y and Z directions are significantly reduced due to intermediate supports. The deflection is always the largest for the h–h case, while the c–c case exhibits the smallest value. However, the maximum deflections of the h–h and c–h cases in Z direction are not significantly different for the two-span shaft in $0<\alpha\leqslant 1.03$ and for the three-span shaft in $0<\alpha\leqslant 1.74$.
2. The maximum deflection in Z direction may occur at any span and near the midpoint of one span, especially for the c–c case. And the maximum deflection will gradually occur toward the left end of the span with increase of α until it transfers to another span, especially for the h–h case. However, the maximum deflection in Y direction always occurs at the first span, and the associated occurring position varies between the ends of the span for varying values of α.
3. The deflection curve along the longitudinal axis in Z direction exhibits several undulations at smaller values of α for the cases of h–h and c–h. And the range of α that causes this phenomenon will become wider as the number of spans increases. However, the c–c case presents the smooth deflection curve.
4. For the multi-span shaft, when the load with high moving speed passes through the span junction, the shaft deflects opposite to the load in the neighborhood of the span junction, especially for the h–h case.
5. The deflection in Z direction is almost not affected by the rotational speed, but the deflection induced by the gyroscopic effect in Y direction is directly proportional to the rotational speed. However, the positions of maximum deflections on the shaft do not vary in both the Y and Z directions.

References

[1] R. Katz, C.W. Lee, A.G. Ulsoy, R.A. Scott, Dynamic response of a rotating shaft subject to a moving load, *Journal of Sound and Vibration* 122 (1988) 131–148.
[2] J.W.Z. Zu, R.P.S. Han, Dynamic response of a spinning Timoshenko beam with general boundary conditions and subjected to a moving load, *ASME Journal of Applied Mechanics* 61 (1994) 152–160.
[3] H.P. Lee, Dynamic response of a rotating Timoshenko shaft subject to axial forces and moving loads, *Journal of Sound and Vibration* 181 (1) (1995) 169–177.
[4] T.N. Shiau, K.H. Huang, W.C. Hsu, Dynamic response and stability of a rotating ball screw under a moving skew load, *Journal of Chinese Society of Mechanical Engineers* 27 (3) (2006) 297–305.
[5] H.S. Zibdeh, H.S. Juma, Dynamic response of a rotating beam subjected to a random moving load, *Journal of Sound and Vibration* 223 (5) (1999) 741–758.
[6] A. Argento, R.A. Scott, Dynamic response of a rotating beam subjected to an accelerating distributed surface force, *Journal of Sound and Vibration* 157 (1992) 221–231.
[7] F.M.A. El-Saeidy, Finite-element dynamic analysis of a rotating shaft with or without nonlinear boundary conditions subject to a moving load, *Nonlinear Dynamics* 21 (2000) 377–408.
[8] H. Ouyang, M. Wang, Dynamics of a rotating shaft subject to a three-directional moving load, *ASME Journal of Vibration and Acoustics* 129 (2007) 386–389.
[9] A. Argento, A spinning beam subjected to a moving deflection dependent load, Part I: response and resonance, *Journal of Sound and Vibration* 182 (1995) 595–615.
[10] A. Argento, H.L. Morano, A spinning beam subjected to a moving deflection dependent load, Part II: parametric resonance, *Journal of Sound and Vibration* 182 (1995) 617–622.
[11] Y.M. Huang, K.K. Chang, Stability analysis of a rotating beam under a moving motion-dependent force, *Journal of Sound and Vibration* 202 (1997) 427–437.

[12] J. Guo, R. Han, Simulating the diameter error due to the dynamic response of a spinning slender shaft in turning operation, *Simulation* 82 (4) (2006) 227–233.
[13] L. Yuan, V.M. Järvenpää, E. Keskinen, M. Cotsaftis, Simulation of roll grinding system dynamics with rotor equations and speed control, *Communications in Nonlinear Science and Numerical Simulation* 7 (2002) 95–106.
[14] T.N. Shiau, J.L. Hwang, A new approach to the dynamic characteristic of undamped rotor-bearing systems, *ASME Journal of Vibration, Acoustics, Stress, and Reliability in Design* 111 (1989) 379–385.
[15] T.N. Shiau, E.C. Chen, K.H. Huang, W.C. Hsu, Dynamic response of a spinning Timoshenko beam with general boundary conditions under a moving skew force using global assumed mode method, *JSME International Journal Series C—Mechanical Systems Machine Elements and Manufacturing* 49 (2) (2006) 401–410.
[16] M. Lalanne, G. Ferraris, *Rotordynamics Prediction in Engineering*, Wiley, New York, 1990.
[17] C.C. Cheng, J.K. Lin, Modelling a rotating shaft subjected to a high-speed moving force, *Journal of Sound and Vibration* 261 (2003) 955–965.